Trace elements discriminate between tissues in highly weathered fossils

Pierre Gueriau[a,b,1], Farid Saleh[a,1], Lukáš Laibl[a,c,d], Francesc Perez Peris[a], Lorenzo Lustri[a], Cristian Mocuta[e], Solenn Réguer[e], Serge X. Cohen[b], Loïc Bertrand[f], and Allison C. Daley[a,1]

[a]Institute of Earth Sciences, University of Lausanne, Géopolis, CH-1015 Lausanne, Switzerland; [b]Université Paris-Saclay, CNRS, ministère de la Culture, UVSQ, MNHN, Institut photonique d'analyse non-destructive européen des matériaux anciens, 91192, Saint-Aubin, France; [c]Czech Academy of Sciences, Institute of Geology, Rozvojová 269, 165 00 Prague 6, Czech Republic; [d]Institute of Geology and Palaeontology, Faculty of Science, Charles University, Albertov 6, Prague, 12843, Czech Republic; [e]Synchrotron SOLEIL, l'Orme des Merisiers, Départementale 128, 91190 Saint-Aubin, France; [f]Université Paris-Saclay, ENS Paris-Saclay, CNRS, Photophysique et Photochimie Supramoléculaires et Macromoléculaires, 91190 Gif-sur-Yvette, France.

[1]To whom correspondence may be addressed. Emails: pierre.gueriau@hotmail.fr, farid.nassim.saleh@gmail.com, or allison.daley@unil.ch

Author Contributions: P.G. and A.C.D. designed the research; P.G., F.S., L.La., F.P.P., L.Lu. C.M. and S.R. performed the research; P.G., C.M., S.R., S.X.C. and L.B. contributed new reagents/analytic tools; P.G., F.S., S.X.C. and L.B. analysed data; P.G. and F.S. wrote the paper with input from all authors.

Keywords: Ordovician | Fezouata Biota | synchrotron X-ray fluorescence | taphonomy | nervous system

ORCID

PG, 0000-0002-7529-3456; FS, 0000-0002-7529-3456; LLa, 0000-0001-9049-3811; FPP, 0000-0002-4526-9308; LLu, 0000-0002-8951-5160; CM, 0000-0001-5540-449X; SR, 0000-0002-7449-0503; SXC, 0000-0003-2435-2417; LB, 0000-0001-6622-9113; ACD, 0000-0001-5369-5879

Abstract

Palaeontologists assess the affinities of fossils using either morphology-based phylogenetic analyses, possibly enhanced by the use of advanced imaging techniques, or the identification of remnants or derivatives of fossil organic molecules with high taxonomic specificity ("biomarkers"). However, these approaches are often of little use for the majority of fossils whose original morphology and chemistry have been severely altered or completely lost during decay, diagenesis and modern weathering. Here we show that the inorganic incorporation of trace elements during fossilization and diagenesis can be used to assess the affinity of highly altered fossils, constituting a powerful tool overlooked so far. This is illustrated by the study of a wide range of animals from the Early Ordovician Fezouata Shale (Tremadocian, Morocco) using synchrotron X-ray fluorescence major-to-trace elemental mapping. Although all fossils studied here have turned into iron oxides, spectral analyses reveal that their different tissue types (i.e. biomineralised, sclerotised, cuticularised, and internal tissues) can be distinguished on the basis of their trace element inventories. The resulting elemental classes and distributions allowed us to identify an enigmatic, highly weathered organism as a new stem euarthropod preserving remains of its nervous system.

Elucidating the origin and evolutionary history of life relies on the accurate placing of organisms, extant and extinct, on the tree of life. This has historically been based upon anatomical similarities, with clades being identified by shared derived characteristics (synapomorphies) that can be traced to a most recent common ancestor and are not present in more distant groups and ancestors. For extant organisms, such phylogenetic/cladistic classifications were revolutionised by molecular biology, which utilizes differences and similarities in genetic sequences, predominately DNA and RNA, to build trees of evolutionary relationships. However, despite being successfully applied to recently extinct animals such as the giant moas from New Zealand[1,2] or the iconic mammoth[3,4], these methods are of limited use for most fossil organisms, because observed rates of DNA degradation indicate that in samples older than 1.5 million years, DNA is either severely crosslinked or non-detectable[5] and the oldest ancient DNA ever extracted (from permafrost-preserved mammoth teeth) is 1.6 million years old[4]. Palaeontology has undergone its own revolution with the advent of 3D X-ray microtomography and more recently a series of advanced 2D imaging techniques, which reveal previously inaccessible or invisible anatomical information[6–12]. These techniques allow fossil anatomy to be described better than ever before, providing a wide range of new characters that have led to better resolution of phylogenetic analyses[13–15]. Furthermore, although DNA is not preserved in ancient fossils, remnants or derivatives of ancient biomolecules can survive in the geological record, associated to organically-preserved fossil remains or isolated within sedimentary rocks[16–26]. Some of these compounds represent biomolecular signatures (or "biomarkers") diagnostic of particular (often broad) clades of organisms, and therefore represent a powerful complement to fossil anatomies in revealing the history of life[20]. Nonetheless, such approaches provide little new information when applied to the majority of fossils whose morphology and chemistry have substantially been altered during decay, burial, diagenesis and weathering. As a result, recent studies focus on relatively "unaltered" specimens while many other fossils remain enigmatic in their affinities. New tools and approaches accounting for and exploiting information loss/gain during the taphonomic history are needed to help deciphering the affinities of altered fossils[20,27,28].

Here we report the major-to-trace elemental composition of 14 strongly weathered fossil animals, including various arthropods, annelids, sponges and an echinoderm, from the Early Ordovician (Tremadocian) Fezouata Shale of Morocco[29,30] using synchrotron-based X-ray fluorescence (XRF) mapping. In this Burgess Shale-type deposit, fossils were originally preserved as carbonaceous compressions and/or in authigenic minerals including pyrite[31,32], before being extensively weathered by modern water circulations that led to the leaching of carbon from carbonaceous compressions, the oxidation of pyrite crystals into yellow, red to purple iron oxide

pseudomorphs, the deposition of new, poorly crystallised Fe-oxides in previously non-pyritised areas, and the dissolution of carbonates from the matrix and from the skeletal elements of animals such as echinoderms[31–34]. We consistently extracted mean XRF spectra from the tissues preserved in our fossils, as well as from their surrounding sedimentary matrix (see Figs. 1*A–M*, Table S1 and Figs. S1–S14 for location and details on the specimens and the selected areas, and methods for the XRF spectra extraction strategy). Linear discriminant analysis (LDA) was then applied to assess systematic variation in the major-to-trace elemental chemistry of different structure types (defined according to Saleh et al.[35]), i.e. between biomineralised, sclerotised, cuticularised, and internal tissues, and the sedimentary matrix. We further show the potential of this framework to interpret the anatomy of a highly weathered enigmatic organism from the Fezouata Biota.

Results and Discussion

Highly weathered fossils preserve tissue-specific trace elemental chemistries.

Our results show that although the fossils have all been extensively weathered to Fe-oxides (usually goethite, more rarely hematite, as determined by Raman spectroscopy), their biomineralised, sclerotised, cuticularised, and internal tissues can still be distinguished based on their trace element composition (Fig. 1*N*). Iron is naturally the main element composing the fossils (as Fe-oxyhydroxides), but it is also the main element probed by our analyses for the surrounding shale (as Fe-bearing clay minerals) because light elements and particularly silicon cannot be detected with the used setup (see Methods). All fossil tissues are, nevertheless, richer in Fe than the shale, and are also considerably enriched in As and Pb (Fig. 1*O*). The proximity of biomineralised and sclerotised tissues in the LDA plot indicates they have a similar elemental composition, only discriminated by a slight enrichment in Ti and Zn in biomineralised tissues, and in Fe, Cu, As and Pb in sclerotised tissues. Cuticularised tissues differ by strong depletions in Cu and As, as well as in Rb, Sr and Y. The only internal tissue available for study contains little to no Ni, Cu, Zn and Ga, and is the most depleted in Rb, Sr and Y. Note that no chemical inventory was collected for soft cellular outer tissues in direct contact with seawater (e.g. tentacles) as they were never found preserved in the Fezouata Biota[32,35].

The specific chemical inventory for each type of tissues can be further confirmed considering that analysed fossils were found in numerous and distant (up to >30 km; Fig. S15) contemporaneous outcrops with different modern-weathering history[31]. This means that the chemical discrimination between different tissue types is not specific to a particular outcrop, and

tissue types can be chemically differentiated within the entire Fezouata Shale, because it was affected by broadly similar water circulation processes in the Draa valley[32]. The high concentrations and chemical speciation of the accessory metals imply that they have accumulated mainly through reactive transport during diagenesis –before the material reaches a stage of depercolation where the formation of specific fluid pathways and remineralisation blocks further uptake– rather than being originally present in the living organism (and persisting through geological times). Indeed, Cu, As, Pb, Ti and Zn concentrations in the 0.02–0.86 wt% range (see Table S2, and Methods for XRF quantification) are exceeding by one to several orders of magnitude those encountered in modern relatives of the Fezouata organisms, even when inhabiting environments heavily contaminated by terrestrial pollutants[37,38]. Furthermore, the most contrasting metal Cu is present in all investigated fossils as a Cu-carbonate compound (Fig. S16), which ubiquitous occurrence in such a wide range of organisms and tissues cannot be original, particularly considering that weathering led to the dissolution of carbonates from skeletal elements of animals such as echinoderms[31–34]. A description of the precise mechanisms responsible for such a diagenetic uptake (i.e. percolation, deposition, adsorption or substitution) is beyond the scope of the present work, but it clearly indicates that tissue-specific physico-chemical differences persisted long enough after decay and early mineralization to distinctly influence later elemental uptake, leading to elemental signatures that were retained (at least locally) after extensive subsequent weathering.

Trace elemental composition can identify tissue types in enigmatic fossils.

Building on this tissue-specific chemical inventory, we used XRF mapping and the obtained LDA classification to interpret the anatomy of an enigmatic, highly weathered organism (AA-FETB-OI-22; Figs. 2*A, B*). While it is particularly challenging to optically investigate this specimen owing to its poorly preserved state, the distributions of Fe (enriched in fossil tissues) (Fig. 2*C*) and to a larger extent Rb (depleted in most fossil tissues) allow us to distinguish the outline of the organism (Fig. 2*D*), which does not include the entire brownish-purplish weathered surface. Chemically, we can distinguish two different types of tissues in this fossil: one depleted in Rb (Fig. 2*D*), and a central, 3-mm wide tubular structure strongly enriched in Fe (Fig. 2*C*), optically yellowish and burgundy in colour, which extends anteriorly into a 28-mm long, yellowish and unsegmented slender appendage that curves along its length and tapers to a pointed end (Figs. 2*B, C*). We extracted mean XRF spectra from these two tissues and the sedimentary matrix (see Fig. 2*C*, Table S1 and Fig. S17 for location and details on the selected areas) and added them to our LDA classification (Fig. 2*E*). The matrix spectrum perfectly clusters with the matrix spectra from the other Fezouata fossils. The composition of the main body part clusters with that of cuticularised tissues. The anterior part of the

Fe-rich tubular structure, however, does not cluster with biomineralised, sclerotised or cuticularised tissues. Its central position is in proximity to the one data point from known internal tissue, making this the most likely tissue type for this tubular structure. The posterior part of this tubular structure, which is more burgundy in colour (Fig. 2*B*) and of different trace elemental composition (richer in Cu and Pb; Fig. 2*F*), plots distinctively from the anterior part, closer to the internal tissue point (Fig. S17), and may therefore represent the remains of another internal system. Note that the richer in iron the XRF spectra extracted from weathered matrix areas are the closer they plot to cuticularised tissues, following the fact that the shale matrix (clay and silica) is way less concentrated in iron than the fossil tissues (Fe-oxyhydroxides) (Fig. S17).

Using the elemental composition as a guide, a description of the overall anatomy of this animal can be made (Fig. 2*G*). The organism has a cuticularised, 11-mm wide, elongated and parallel-side trunk region, through which runs a central 3-mm wide band of internal tissues that extends into a 28-mm long slender, tapering and unsegmented appendage. The trunk region shows several faint discontinuous parallel lines that suggest the body was segmented and divided into a minimum of 6 body units. Laterally to the trunk outline, the cuticularised tissues extend outwards into poorly-defined wide lateral flaps that are rounded or roughly triangular in outline. This combination of anatomical features is very reminiscent of *Kerygmachela kierkegaardi*, a stem-group euarthropod from the Cambrian Sirius Passet Biota of Greenland[39,40]. An affinity for the Fezouata Shale organism similar to *K. kierkegaardi* would suggest that one of the pair of frontal appendages has not been preserved in the Fezouata organism, explaining the asymmetrical position of the one that is present. Regardless, due to the 40 Myr gap between the Sirius Passet and the Fezouata Shale, it is unlikely that the Fezouata organism belongs to the same taxon. In any case, stem euarthropod affinities for this organism increase the species richness of the Fezouata Biota.

A closer look at the regions of the specimen interpreted as internal tissues reveals anatomical detail that allows us to identify the organ systems that are present. Microscopic examination of the anterior yellowish region of the internal tissues reveals the presence, besides numerous rock fractures, of lateral extensions (Fig. 3*A*). A higher-resolution XRF map (25-µm pixel size) further unveils four Fe-rich spherical structures organised antero-posteriorly, as well as another pair of two spherical structures, not as rich in Fe, positioned laterally to the first spherical structure and connected to it by an elbow duct (Figs. 3*B,C*). The only interpretation for such an arrangement of structures is that they represent four ganglia of the nervous system and a pair of lateral eyes, respectively (Fig. 3*C,D*). Although rare, the fossilisation of nervous tissues is being documented in a growing number of fossils[40–49]. It is explained by the presence of highly reactive biogenic Fe in the nervous system, which has been proposed to initiate selective pyritisation very rapidly during

early diagenesis while other tissues are still decaying[50]. Nonetheless, the undisputable identification of fossilised internal anatomical features as remains of nervous tissues may be challenging. Aria et al. proposed a set of criteria for their recognition, namely the consideration of the specimen topology, the morphoanatomical consistency, the taphonomic context and redundancy[51]. The remains observed in AA-FETB-OI-22 meet most of the proposed criteria: surface relief has been carefully considered, as shown in our interpretative drawing (Fig. 3*C*), especially as the Fe distribution probed by XRF is not limited to the surface (see Methods) allowing us to confidently distinguish between relief and fossilised remains; features are consistent with those described from closely-related fossils[40]; detailed knowledge of the taphonomy at the site[31–35] and the dorso-ventral plane of preservation associated with some 3D preservation uncovered by XRF ensure that taphonomic variations have been considered. We, however, acknowledge that the redundancy criterion is not met, but we argue that if our method could uncover such new features in a random specimen then more are expected to be discovered. The internal anatomical features preserved in the analysed specimen therefore represent the first remains of a nervous system ever reported from the Ordovician period. The other regions of the internal tubular structure that have a different chemistry (Fig. 2*F*) likely represent remains of other internal tissues or systems (Fig. 2*G*).

Towards a more exhaustive documentation of the history of life

The identification, based upon the tissue-specific incorporation of inorganic minor and trace elements, of a stem euarthropod yielding remains of the nervous system from Fezouata extends both its biodiversity and the range of tissues that could be preserved there. It also illustrates the potential of novel uses of advanced spectro-imaging techniques to identify pivotal yet poorly preserved and/or highly weathered fossils such as lower stem euarthropods, which are neither biomineralised nor sclerotised and as such have a low fossilisation potential.

Tissue-specific chemistry is known to be a powerful tool for interpreting the soft tissue anatomy of exceptionally preserved fossils. This approach has been developed with XRF mapping of a wide range of vertebrates retaining organometallic compounds derived from the original melanin pigments[52–54]. Recently, the discovery that tissue-specific chemical signatures can persist in fossilised internal melanosomes (quite common in the fossil record) has even suggested that it could potentially be used to constrain the affinities of enigmatic fossil vertebrates[55]. Yet, such an approach is limited to literally exceptionally preserved fossils, i.e. retaining molecular and/or organelles remains, which have only been affected by limited diagenetic[55–57]. In the case of most other fossils, which only preserve hard parts bones, shells, plates, ossicles, biomineralised cuticle), and occasionally soft parts replicated in minerals during fossilisation and/or, diagenesis, the use of XRF

mapping has been limited to acquiring chemical information and visualising anatomical features superficially hidden beneath the sample surface[10,11,58–60]. Our study unexpectedly shows that the combination of both the spatial and chemical information provided by elemental mapping with appropriate sampling and data processing can represent, for a given locality, a powerful toolkit to decipher the anatomy and affinities of poorly preserved and/or highly weathered soft-bodied fossils. Documenting new anatomical features completes our knowledge of past biodiversity and ecology, while uncovering hidden evolutionary patterns. As such, this approach holds great promise in allowing a detailed understanding of overlooked aspects of the history of life.

Materials and Methods

Fossil specimens. The studied material is housed in the collections of the Musée cantonal de Géologie de Lausanne (MGL), and of the Cadi-Ayyad University (Faculté des Sciences et Techniques, Guéliz), Marrakesh, Morocco. The MGL material was collected by authorised and academically recognised avocational Moroccan collector Mohamed Ben Moula and his family over the period of 2015 to 2016; A.C.D. worked in collaboration with them to collect the metadata associated with the collected fossils. Mohamed Ben Moula has a long-standing working relationship with several academics, has received the Mary Anning Award from the Palaeontological Association, and has a radiodont fossil named after him in honour of his great contribution to the field of palaeontology. The collection was purchased with funds from the University of Lausanne and the Swiss National Science Foundation, following all regulations for purchases. The material was transported to Casablanca and subjected to export approval by the Ministry of Energy, Mines and the Environment of the federal government of the Kingdom of Morocco and approved for shipment to Switzerland on 11.05.2017 (export permits curated with the collection). The material from the Marrakesh collection studied herein was loaned to the University Lyon 1 for study and will be returned to the Cadi-Ayyad University after study.

Details about the fossil specimens investigated herein (identification, inventory numbers, and localities) are given in Table S1. Precise locality information is curated with the specimens, and available upon request from the authors. Specimens were selected to represent a variety of taxa and tissue types, for which remains are thicker than 300 µm to make sure that the elemental signal recorded using µXRF only comes from the fossil itself and not also from the underlying sedimentary matrix. Details about the scanning steps and dwell times used for each map, as well as about the areas from which spectra have been extracted are also given in Table S1.

Elemental mapping. Synchrotron micro X-ray fluorescence (μXRF) major-to-trace elemental mapping was performed at the DiffAbs beamline of the SOLEIL synchrotron source (France), using a monochromatic beam of 18 keV ($\Delta E/E \sim 1–2\times10^{-4}$), selected for excitation of K-lines from phosphorus to yttrium and L-lines from cadmium to uranium. In order to map the specimen with a high lateral resolution, the beam was reduced down to a diameter of 50 μm using a molybdenum pinhole. The sample was mounted on a scanner stage allowing 90 mm movements (in both horizontal and vertical directions) with micrometre accuracy, and orientated at 45° with respect to the incident beam. XRF was collected using a 4-element silicon drift detector (SDD, Vortex ME4, Hitachi High-Technologies Science America, Inc., total active area: 170 mm^2) oriented at 90° with respect to the incident beam, in the horizontal plane[11] in order to minimize the elastic (Thompson) scattering signal.

Two-dimensional spectral images, *i.e.* images for which each pixel is characterised by a full XRF spectrum, were collected *on the fly*[61] over the specimens at a 20–200 μm lateral resolution with a 20–70 ms dwell time (effective counting time was 90% of the dwell time) depending on the samples (see Table S1 for the precise scanning steps and dwell times used for each map). Spectra were then reduced by summing intensities from the four elements of the XRF detector, and integrating intensities every 100 eV. All elemental distributions presented herein correspond to integrated intensities from the main XRF peaks, produced using ImageJ and represented using grey, RGB composite or Green Fire Blue colour scales.

XRF spectra extraction. Based on the obtained elemental distributions, we consistently extracted mean XRF spectra from the different tissues preserved in our fossils, as well as from their surrounding sedimentary matrix, carefully selecting homogeneous areas (see Figs. 1*A–M*, Table S1 and Figs. S1–S14 for location and details on the specimens and the selected areas). We particularly avoided Mn-rich areas that resulted from recent weathering and covered parts of some fossils (Figs. 1*D, G* and *L*) as they would obscure other chemical signals; weathering in the Fezouata Shale was also responsible for the leaching of carbon, oxidation of pyrite, deposition of Fe-oxides and dissolution of carbonates[31–34]. To compensate for the use of different exposure times between datasets, the number of pixels for each area was adapted such that the collection time (and consequently the signal-to-noise ratio) was similar between all extracted spectra (see Table S1). Another important parameter to consider is the thickness of the fossil material. At 18 keV, the attenuation length for goethite (the main iron oxyhydroxide in the Fezouata fossils) is about 80 μm: it is therefore essential that extracted spectra are collected from fossil tissues thicker than this

length, so that the extracted signal is not the sum of contributions from the fossil and the underlying sediment.

Linear discriminant analyses. Differences in elemental abundances between the tissue types of the 14 identified fossils were assessed using a linear discriminant analysis (LDA), a method that explains (and predicts) the affiliation of an individual to a predefined class (group) based on the measured predictive variable characteristics. The analyses were performed in the R statistical environment using the `MASS` package[62], and plotted using the `ggplot2` package[63]. The statistical analysis is based on the integrated intensity of the XRF signals of the different elements, with partial reabsorption by the matrix. To discriminate between tissues, we directly rely on the fact that the signal results from the statistical realisation of the photon-matter interaction (rather than quantitative estimates). Discrimination therefore takes into account both the average content in each element and its local distribution within each probed voxel (containing material of varying composition). Prior to the LDA, bending followed by a rubberband baseline corrections were applied to the log-normalised spectra using the `wl.eval` and `spc.rubberband` function of the `hyperSpec` package[64]. Spectra from the enigmatic organism were then added to the LDA plot using the `predict` function. Spectra and the R script used in this work are available via the following Dryad Digital Repository:
https://datadryad.org/stash/share/LGEGhXAwq2FZjiDl2k9MPFfZ1D0Vt0Z_M1wLWXSKzSw
(private, randomized URL for Peer Review until the related manuscript has been accepted).

XRF quantification. Full quantification of trace elements from XRF maps of heterogeneous materials such as fossils is generally hampered by local heterogeneity (both laterally and in depth), which limits the precision of corrections for matrix X-ray reabsorption, with strong impact on the calculated concentrations depending on the hypothesis on the matrix composition. Nonetheless, by carefully selecting homogeneous areas (based on elemental distributions) and defining the matrix, statistics are sufficient to estimate semi-quantitative contents of trace elements in fossils[65,66]. We estimated elemental concentrations in our fossils from a full spectral decomposition performed with the PyMCA data analysis software[67] using an Hypermet peak shape, a polynomial approximation of the baseline and experimental parameters, applying reabsorption corrections considering a goethite matrix (as determined by Raman spectroscopy). The photon flux was estimated to 3.4×10^{9} photons•s^{-1} taking Fe as internal standard (62.85wt% in pure goethite). Resulting concentrations expressed as wt% are presented in Table S2.

Acknowledgments

We are grateful to SOLEIL synchrotron for provision of beamtime, D. Thiaudière, and P. Joly for assistance at the DiffAbs beamline, as well as B. Lefebvre and E. Robert for facilitating access to the material from the Marrakesh collection, and G. Potin for help with the Musée cantonal de Géologie de Lausanne collection. P.G., F.P.P., L.Lu. and this research were funded by the Swiss National Science Foundation, grant number 205321_179084 entitled "Arthropod Evolution during the Ordovician Radiation: Insights from the Fezouata Biota" and awarded to A.C.D. L.La. was supported by the Center for Geosphere Dynamics (UNCE/SCI/006), and by the institutional support RVO 67985831 of the Institute of Geology of the Czech Academy of Sciences. F.S. acknowledges funding from the Faculty of Geosciences and Environment of the University of Lausanne.

References

1. A. Cooper, C. Mourer-Chauviré, G. K. Chambers, A. von Haeseler, A. C. Wilson, S. Pääbo, Independent origins of New Zealand moas and kiwis. *Proc. Natl. Acad. Sci. U.S.A.* **89**, 8741-8744 (1992).
2. A. J. Baker, L. J. Huynen, O. Haddrath, C. D. Millar, D. M. Lambert, Reconstructing the tempo and mode of evolution in an extinct clade of birds with ancient DNA: the giant moas of New Zealand. *Proc. Natl. Acad. Sci. U.S.A.* **102**, 8257-8262 (2005).
3. R. Debruyne, V. Barriel, P. Tassy, Mitochondrial cytochrome *b* of the Lyakhov mammoth (Proboscidea, Mammalia): new data and phylogenetic analyses of Elephantidae. *Mol. Phylogenet. Evol.* **26**, 421–434 (2003).
4. T. van der Valk, P. Pečnerová, D. Díez-del-Molino, A. Bergström, J. Oppenheimer *et al.* Million-year-old DNA sheds light on the genomic history of mammoths. *Nature* **591**, 265–269 (2021).
5. E. Willerslev, A. J. Hansen, R. Rønn, T. B. Brand, I. Barnes, C. Wiuf, D. Gilichinsky, D. Mitchell, A. Cooper, Long-term persistence of bacterial DNA. *Curr. Biol.* **14**, R9–R10 (2004).
6. P. Tafforeau, R. Boistel, E. Boller, A. Bravin, M. Brunet *et al.*, Applications of X-ray synchrotron microtomography for non-destructive 3D studies of paleontological specimens. *Appl. Phys. A* **83**, 195–202 (2006).
7. S. Y. Smith, M. E. Collinson, P. J. Rudall, D. A. Simpson, F. Marone, M. Stampanoni, Virtual taphonomy using synchrotron tomographic microscopy reveals cryptic features and internal structure of modern and fossil plants. *Proc. Natl. Acad. Sci. U.S.A.* **106**, 12013-12018 (2009).
8. U. Bergmann, R. W. Morton, P. L. Manning, W. I. Sellers, S. Farrar, K. G. Huntley, R. A. Wogelius, P. L. Larson, *Archaeopteryx* feathers and bone chemistry fully revealed via synchrotron imaging. *Proc. Natl. Acad. Sci. U.S.A.* **107**, 9060–9065 (2010).
9. U. Bergmann, L. Bertrand, N. P. Edwards, P. L. Manning, R. A. Wogelius,"Chemical mapping of ancient artifacts and fossils with x-ray spectroscopy" in *Synchrotron Light*

Sources and Free-Electron Lasers: Accelerator Physics, Instrumentation and Science Applications, E. Jaeschke, S. Khan, J. R. Schneider, J. B. Hastings, Eds. (Springer Nature Swizterland, 2019).
10. P. Gueriau, C. Mocuta, D. B. Dutheil, S. X. Cohen, D. Thiaudière, The OT1 Consortium, S. Charbonnier, G. Clément, L. Bertrand, Trace elemental imaging of rare earth elements discriminates tissues at microscale in flat fossils. *PLoS One* **9**, e86946 (2014).
11. P. Gueriau, C. Jauvion, C Mocuta, Show me your yttrium, and I will tell you who you are: implications for fossil imaging. *Palaeontology* **61**, 981–990 (2018).
12. T. G. Kaye, A. R. Falk, M. Pittman, P. C. Sereno, L. D. Martin, D. A Burnham, E. Gong, X. Xu, Y. Wang, Laser-Stimulated Fluorescence in Paleontology. *PLoS One* **10**, e0125923 (2015).
13. S. Giles, M. Friedman, M. Brazeau, Osteichthyan-like cranial conditions in an Early Devonian stem gnathostome. *Nature* **520,** 82–85 (2015).
14. D. Zhai, J. Ortega-Hernández, J. M. Wolfe, X. Hou, C. Cao, Y. Liu, Three-dimensionally preserved appendages in an Early Cambrian stem-group pancrustacean. *Curr. Biol.* **29**, 171–177 (2019).
15. T. Miyashita, M. I. Coates, R. Farrar, P. Larson, P. L. Manning, R. A. Wogelius, N. P. Edwards, J. Anné, U. Bergmann, A. R. Palmer, P. J. Currie, Hagfish from the Cretaceous Tethys Sea and a reconciliation of the morphological–molecular conflict in early vertebrate phylogeny. *Proc. Natl. Acad. Sci. U.S.A.* **116**, 2146–2151 (2019).
16. J. J. Brocks, R. E. Summons, Sedimentary Hydrocarbons. *Biogeochemistry* **8**, 63–115 (2005).
17. J. J. Brocks, A. Pearson, Building the biomarker tree of life. *Rev. Mineral. Geochem.* **59**, 233–258 (2005).
18. J. Lindgren, P. Uvdal, P. Sjövall, D. E. Nilsson, A. Engdahl *et al.*, Molecular preservation of the pigment melanin in fossil melanosomes. *Nat. Communications* **3**, 824 (2012).
19. D. E. Greenwalt, Y. S. Goreva, S. M. Siljeström, T. Rose, R. E. Harbach, Hemoglobin-derived porphyrins preserved in a Middle Eocene blood-engorged mosquito. *Proc. Natl. Acad. Sci. U.S.A.* **110**, 18496–18500 (2013).
20. D. E. G. Briggs, R. Summons, Ancient biomolecules: their origins, fossilization, and role in revealing the history of life. *BioEssays* **36**, 482–490 (2014).
21. C. Colleary, A. Dolocan, J. Gardner, S. Singh, M. Wuttke *et al.*, Chemical, experimental, and morphological evidence for diagenetically altered melanin in exceptionally preserved fossils. *Proc. Natl. Acad. Sci. U.S.A.* **112**, 12592–12597 (2015).
22. Y. Pan, W. Zheng, A. E. Moyer, J. K. O'Connor, M. Wang *et al.*, Molecular evidence of keratin and melanosomes in feathers of the Early Cretaceous bird *Eoconfuciusornis*. *Proc. Natl. Acad. Sci. U.S.A.* **113**, E7900–E7907 (2016).
23. V. Vajda, M. Pucetaite, S. McLoughlin, A. Engdahl, J. Heimdal, P. Uvdal, Molecular signatures of fossil leaves provide unexpected new evidence for extinct plant relationships. *Nat. Ecol. Evol.* **1**, 1093–1099 (2017).
24. I. Bobrovskiy, J. M. Hope, A. Ivantsov, B. J. Nettersheim, C. Hallmann, J. J. Brocks, Ancient steroids establish the Ediacaran fossil *Dickinsonia* as one of the earliest animals. *Science* **361**, 1246–1249 (2018).

406 25. Y. Pan, W. Zheng, R. H. Sawyer, M. W. Pennington, X. Zheng *et al.*, The molecular
407 evolution of feathers with direct evidence from fossils. *Proc. Natl. Acad. Sci. U.S.A.* **116**,
408 3018–3023 (2019).
409 26. K. H. Kjær, M. Winther Pedersen, B. De Sanctis, B. De Cahsan, T. S. Korneliussen *et al.,* A
410 2-million-year-old ecosystem in Greenland uncovered by environmental DNA. *Nature* **612**,
411 283–291 (2022).
412 27. D. J. Murdock, S. E. Gabbott, M. A. Purnell M.A., The impact of taphonomic data on
413 phylogenetic resolution: *Helenodora inopinata* (Carboniferous, Mazon Creek Lagerstätte)
414 and the onychophoran stem lineage. *BMC Evol. Biol.* **16**, 19 (2016).
415 28. L. Bertrand, M. Thoury, P. Gueriau, É. Anheim, S. Cohen, Deciphering the Chemistry of
416 Cultural Heritage: Targeting Material Properties by Coupling Spectral Imaging with Image
417 Analysis. *Acc. Chem. Res.* **54**, 19670–19676 (2021).
418 29. P. Van Roy, P. J. Orr, J. P. Botting, L. A. Muir, J. Vinther, B. Lefebvre, K. El Hariri, D. E.
419 G. Briggs, Ordovician faunas of Burgess Shale type. *Nature* **465**, 215–218 (2010).
420 30. P. Van Roy, D. E. G. Briggs, R. R. Gaines, The Fezouata fossils of Morocco; an
421 extraordinary record of marine life in the Early Ordovician. *J. Geol. Soc.* **172**, 541–549
422 (2015).
423 31. F. Saleh, B. Pittet, P. Sansjofre, P. Gueriau, S. Lalonde *et al.*, Taphonomic pathway of
424 exceptionally preserved fossils in the Lower Ordovician of Morocco. *Geobios* **60**, 99–115
425 (2020).
426 32. F. Saleh, R. Vaucher, J. B. Antcliffe, A. C. Daley, K. El Hariri *et al.*, Insights into soft-part
427 preservation from the Early Ordovician Fezouata Biota. *Earth-Science Reviews* **213**, 103464
428 (2021).
429 33. B. Lefebvre, T. E. Guensburg, E. L. O. Martin, R. Mooi, E. Nardin *et al.*, Exceptionally
430 preserved soft parts in fossils from the Lower Ordovician of Morocco clarify stylophoran
431 affinities within basal deuterostomes. *Geobios* **52**, 27–36 (2019).
432 34. F. Saleh, B. Lefebvre, A. W. Hunter, M. Nohejlov, Fossil weathering and preparation mimic
433 soft tissues in eocrinoid and somasteroid echinoderms from the Lower Ordovician of
434 Morocco. *Microscopy today* **28**, 24–28 (2020).
435 35. F. Saleh, J. B. Antcliffe, B. Lefebvre, B. Pittet, L. Laibl *et al.*, Taphonomic bias in
436 exceptionally preserved biotas. *Earth and Planetary Science Letters* **529**, 115873 (2020).
437 36. P. Brouwer, *Theory of XRF* (PANalytical B.V., Almelo, The Netherlands, 2006).
438 37. J. Burger, C. Dixon, T. Shukla, N. Tsipoura, M. Gochfeld, Metal levels in horseshoe crabs
439 (*Limulus polyphemus*) from Maine to Florida. *Environmental research* **90**, 227–236 (2002).
440 38. Q. Liu, X. Xu, J. Zeng, X. Shi, Y. Liao *et al.*, Heavy metal concentrations in commercial
441 marine organisms from Xiangshan Bay, China, and the potential health risks. *Marine*
442 *pollution bulletin* **141**, 215-226 (2019).
443 39. G. B. Budd, A Cambrian gilled lobopod from Greenland. *Nature* **364**, 709–711 (1993).
444 40. T.-Y. S. Park, J.-H. Kihm, J. Woo, C. Park, W. Y. Lee, M. P. Smith, D. A. T. Harper, F.
445 Young, A. T. Nielsen, J. Vinther, Brain and eyes of *Kerygmachela* reveal protocerebral
446 ancestry of the panarthropod head. Nature Communications **9**, 1019 (2018).
447 41. X. Ma, X. Hou, G. D. Edgecombe, N. J. Strausfeld, Complex brain and optic lobes in an
448 early Cambrian arthropod. *Nature* **490**, 258–261 (2012).

42. G. Tanaka, X. Hou, X. Ma, G. D. Edgecombe, N. J. Strausfeld, Chelicerate neural ground pattern in a Cambrian great appendage arthropod. *Nature* **502**, 364–367 (2013).
43. P. Cong, X. Ma, X. Hou, G. D., Edgecombe, N. J. Strausfeld, Brain structure resolves the segmental affinity of anomalocaridid appendages. *Nature* **513**, 538–542 (2014).
44. J. Yang, J. Ortega-Hernández, N. J. Butterfield, Y. Liu,G. S. Boyan, J.-b. Hou, T. Lan, X.-g. Zhang, Fuxianhuiid ventral nerve cord and early nervous system evolution in Panarthropoda. *Proc. Natl. Acad. Sci. U.S.A.* **113**, 2988–2993 (2016).
45. L. Parry, J. B. Caron, *Canadia spinosa* and the early evolution of the annelid nervous system. *Science advances* **5**, eaax5858 (2019).
46. T. Lan, Y. Zhao, F. Zhao, Y. He, P. Martinez, N. J. Strausfeld, Leanchoiliidae reveals the ancestral organization of the stem euarthropod brain. *Current Biology* **31**, 4397–4404 (2021).
47. J. Ortega-Hernández, R. Lerosey-Aubril, S. R. Losso, J. C. Weaver, Neuroanatomy in a middle Cambrian mollisoniid and the ancestral nervous system organization of chelicerates. *Nature communications* **13**, 410 (2022).
48. N. J. Strausfeld, X. Hou, M. E. Sayre, F. Hirth, The lower Cambrian lobopodian *Cardiodictyon* resolves the origin of euarthropod brains. *Science* **378**, 905–909 (2022).
49. R. T. Figueroa, D. Goodvin, M. A. Kolmann, M. I. Coates, A. M. Caron, M.Friedman, S. Giles, Exceptional fossil preservation and evolution of the ray-finned fish brain. *Nature* (2023). https://doi.org/10.1038/s41586-022-05666-1.
50. F. Saleh, A. C. Daley, B. Lefebvre, B. Pittet, J. P. Perrillat, Biogenic iron preserves structures during fossilization: a hypothesis: iron from decaying tissues may stabilize their morphology in the fossil record. *BioEssays* **42**, 1900243 (2020).
51. C. Aria, J. Vannier, J., T. Y. S. Park, R. R. Gaines, Interpreting fossilized nervous tissues. *BioEssays* (2023). https://doi.org/10.1002/bies.202200167.
52. R. A. Wogelius, P. L. Manning, H. E. Barden, N. P. Edwards, S. M. Webb, W. I. Sellers, K. G. Taylor, P. L. Larson, P. Dodson, H. You, L. Da-qing, U. Bergmann, Trace metals as biomarkers for eumelanin pigment in the fossil record. *Science* **333**, 1622–1626 (2011).
53. V. M. Egerton, R. A. Wogelius, M. A., Norell, N. P. Edwards, W. I. Sellers, U. Bergmann, D. Sokaras, R. Alonso-Mori, K. Ignatyev, A. van Veelen, J. Anné, B. E. van Dongen, F. Knoll, P. L. Manning, The mapping and differentiation of biological and environmental elemental signatures in the fossil remains of a 50 million year old bird. *Journal of Analytical Atomic Spectrometry* **30**, 627–634 (2015).
54. P. L. Manning, N. P. Edwards, U. Bergmann, J. Anné, W. I. Sellers, A. van Veelen, D. Sokaras, V. M. Egerton, R. Alonso-Mori, K. Ignatyev, B. E. van Dongen, K. Wakamatsu, S. Ito, F. Knoll, R. A. Wogelius, Pheomelanin pigment remnants mapped in fossils of an extinct mammal. *Nature Communications* **10**, 2250 (2019).
55. V. Rossi, M. E. McNamara, S. M. Webb, S. Ito, K. Wakamatsu, Tissue-specific geometry and chemistry of modern and fossilized melanosomes reveal internal anatomy of extinct vertebrates. *Proc. Natl. Acad. Sci. U.S.A.* **116**, 17880–17889 (2019).
56. V. Rossi, S. M. Webb, M. E. McNamara, Hierarchical biota-level and taxonomic controls on the chemistry of fossil melanosomes revealed using synchrotron X-ray fluorescence. *Scientific Reports* **10**, 8970 (2020).

57. V. Rossi, S. M. Webb, M. E. McNamara, Maturation experiments reveal bias in the chemistry of fossil melanosomes. *Geology* **49**, 784–788 (2021).
58. A. Brayard, P. Gueriau, M. Thoury, G. Escarguel, the Paris Biota team, Glow in the dark: Use of synchrotron μXRF trace elemental mapping and multispectral macro-imaging on fossils from the Paris Biota (Bear Lake County, Idaho, USA). *Geobios* **54**, 71–79 (2019).
59. T. Saucède, E. Vennin, E. Fara, N. Olivier, the Paris Biota team, A new holocrinid (Articulata) from the Paris Biota (Bear Lake County, Idaho, USA) highlights the high diversity of Early Triassic crinoids. *Geobios* **54**, 45–53 (2019).
60. P. Gueriau, J. C., Lamsdell, R. A. Wogelius, P. L. Manning, V. M. Egerton, U. Bergmann, L. Bertrand, J. Denayer, A new Devonian euthycarcinoid evidences the use of different respiratory strategies during the marine-to-terrestrial transition in the myriapod lineage. *Royal Society Open Science* **7**, 201037 (2020).
61. N. Leclercq, J. Berthault, F. Langlois, S. Le, S. Poirier, J. Bisou, F. Blache, K. Medjoubi, C Mocuta, Flyscan: a fast and multi-technique data acquisition platform for the SOLEIL beamlines. *ICALEPCS 2015, the 15th International Conference on Accelerator and Large Experimental Control Systems*, 17–23 October 2015, Melbourne, Australia, Abstract No. WEPGF056 (2015).
62. W. N. Venables, B. D. Ripley, *Modern Applied Statistics with S* (Springer-Verlag New York, 2002).
63. H. Wickham, *ggplot2: Elegant Graphics for Data Analysis* (Springer-Verlag New York, 2016).
64. C. Beleites, V. Sergo, hyperSpec: a package to handle hyperspectral data sets in R, *R package version 0.99-20201127*. (https://github.com/cbeleites/hyperSpec) (2020).
65. P. Gueriau, C. Mocuta, L. Bertrand, Cerium anomaly at microscale in fossils. *Analytical Chemistry* **87**, 8827–8836 (2015).
66. P. Gueriau, S. Bernard, F. Farges, C. Mocuta, D. B. Dutheil *et al.*, Oxidative conditions can lead to exceptional preservation through phosphatization. *Geology* **48**, 1164–1168 (2020).
67. V. A. Solé, E. Papillon, M. Cotte, P. Walter, J. Susini, A multiplatform code for the analysis of energy-dispersive X-ray fluorescence spectra. *Spectrochimica Acta Part B: Atomic Spectroscopy* **62**, 63–68 (2007).

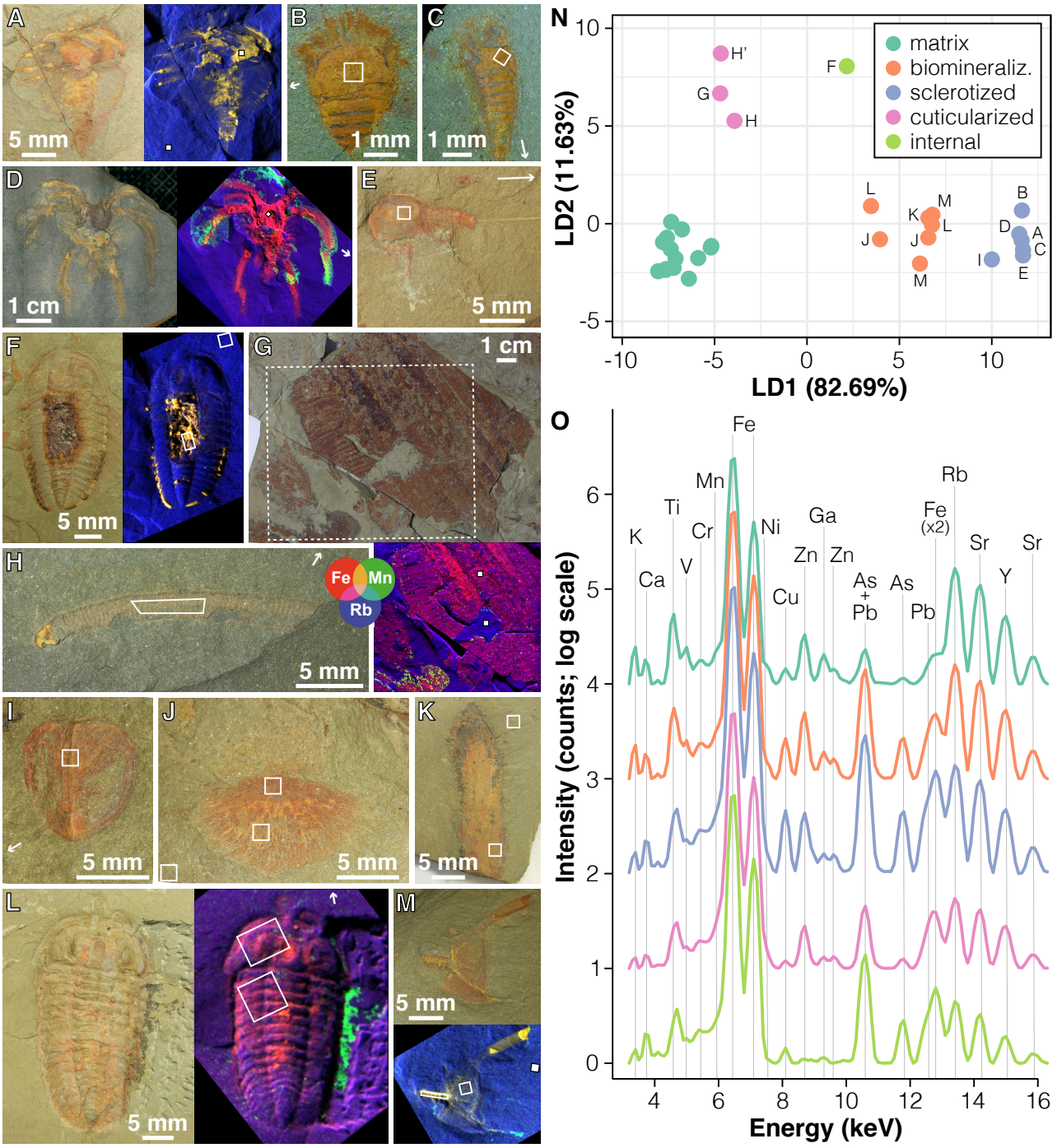

Figure 1. Synchrotron-based XRF major-to-trace elemental mapping of 14 fossil animals from the Early Ordovician Fezouata Shale of Morocco. (*A–M*) Optical photograph and false-colour overlays of iron (red), manganese (green), and rubidium (blue) distributions of the analysed fossils (see Table S1 for specimen details and acquisition parameters). (*N*) Linear discriminant analysis of the mean XRF spectra extracted from the white box areas in *A–M*; white arrows locate spectra for the shale matrix that were taken outside of the displayed field of view, their length being proportional to the distance from the sampled area (see Figs. S1–S14 for precise locations). (*O*) Mean XRF spectrum for each tissue type and the matrix, vertically shifted for readability. The 'Fe ×2' peak in the fossil spectra corresponds to a Fe pile-up peak, an artefactual peak[36] that increases with concentration and further indicate that fossil tissues are richer in Fe than the shale. **[planned for 2-column width]**

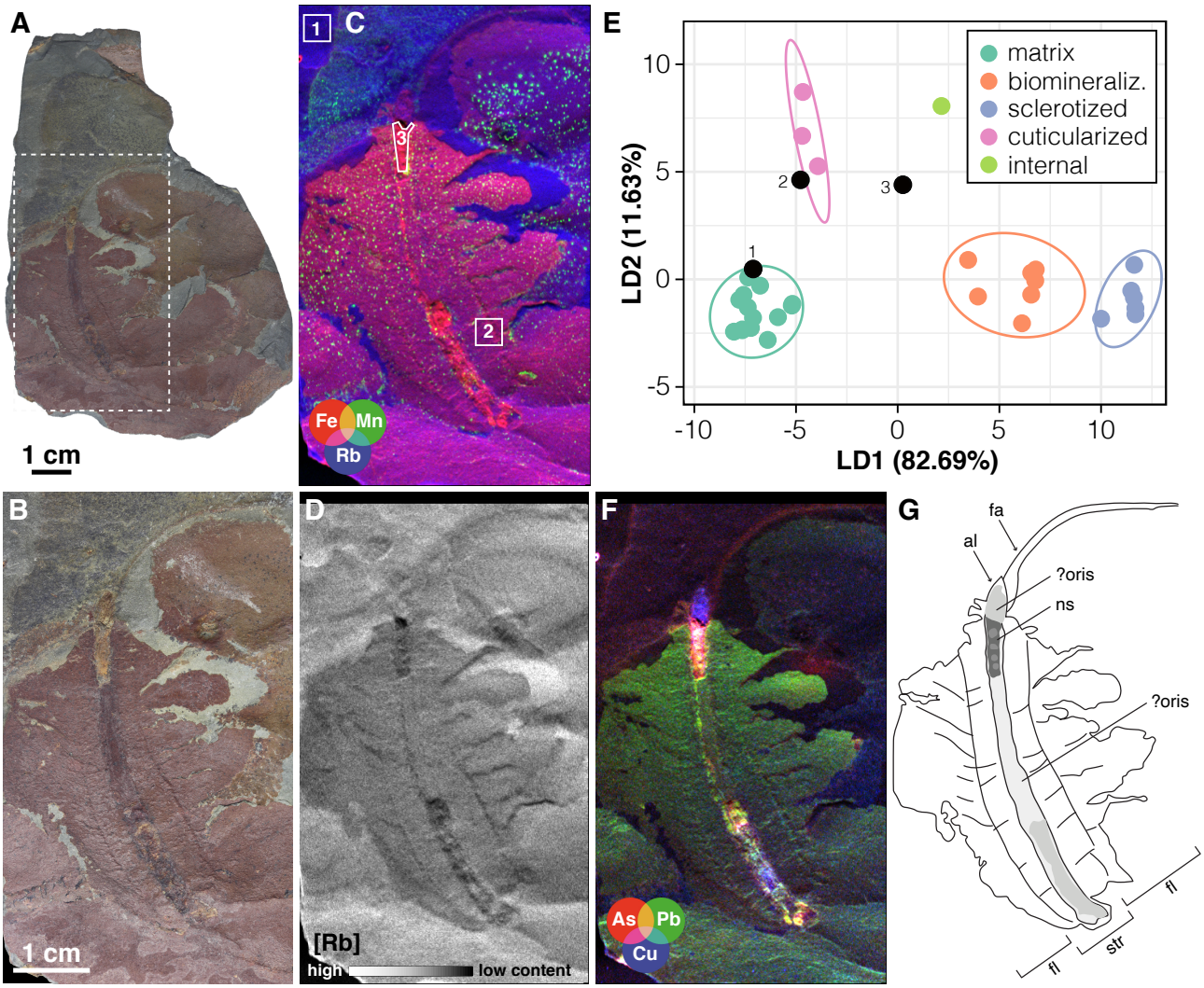

Figure 2. Synchrotron-based XRF major-to-trace elemental mapping of a highly weathered organism (AA-FETB-OI-22) from the Early Ordovician Fezouata Shale of Morocco. (*A*) Optical photograph of the entire slab. (*B*) Close-up on the specimen, from the dotted white box area in *A*. (*C*) False-colour overlay of iron (red), manganese (green), and rubidium (blue) distributions from the area in *B*. Acquisition parameters: 100×100 µm^2 scan step, 20 ms dwell time, 215 280 pixels. Numbered white box areas indicate location of XRF spectra in *E*. (*D*) Rubidium distribution only. (*E*) Classification of the mean XRF spectra extracted from the white box areas in *C* within our LDA. (*F*) False-colour overlay of arsenic (red), lead (green), and copper (blue) distributions. (*G*) Interpretative line drawing of the anatomy of the specimen. Abbreviations: al, anterior lobe; fa, frontal appendage; fl, lateral flaps; ns, nervous system; ?oris, other remains of internal system(s); str, segmented trunk.

[planned for 2-column width]

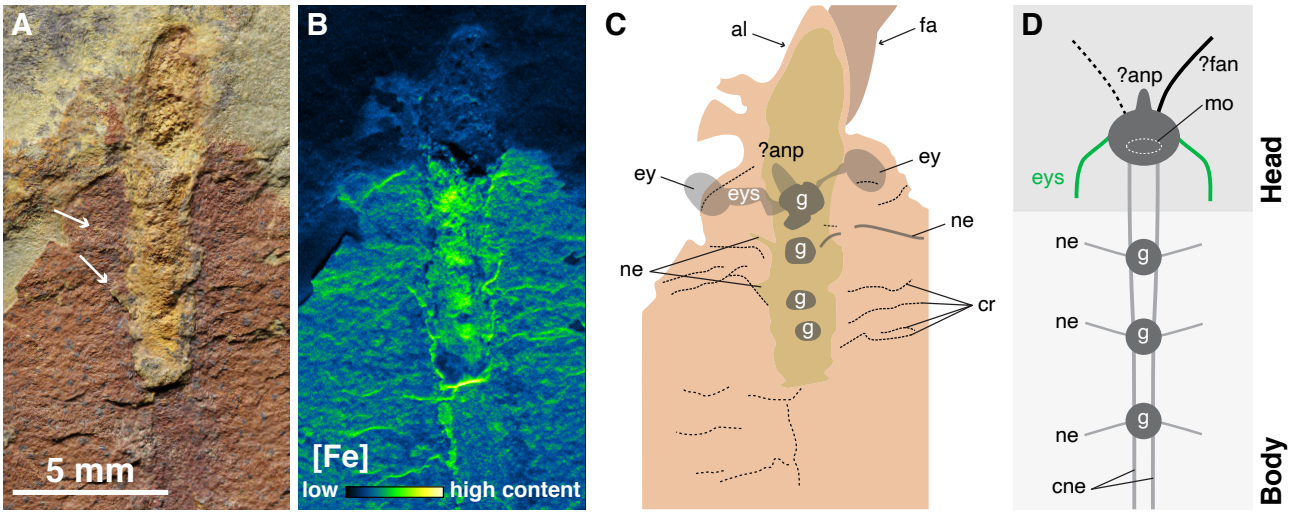

Figure 3. Remains of the nervous system in AA-FETB-OI-22. (*A*) Close-up optical photograph of the head and anteriormost portion of the body. Arrows highlight lateral extensions of the yellowish region. (*B*) Iron distribution (XRF contrast map). Acquisition parameters: 25×25 µm^2 scan step, 20 ms dwell time, 264 163 pixels. (*C*) Interpretative line drawing. (*D*) Schematic reconstructed of the nervous system. Abbreviations: al, anterior lobe; anp, anterior neural projection, cne, central nerves, cr, cracks; ey, eye; eys, eye stalk; g, ganglion; fa, frontal appendage; fan, frontal appendage nerves; mo, mouth; ne, nerves.

[planned for 2-column width]

Extended Data Figures.

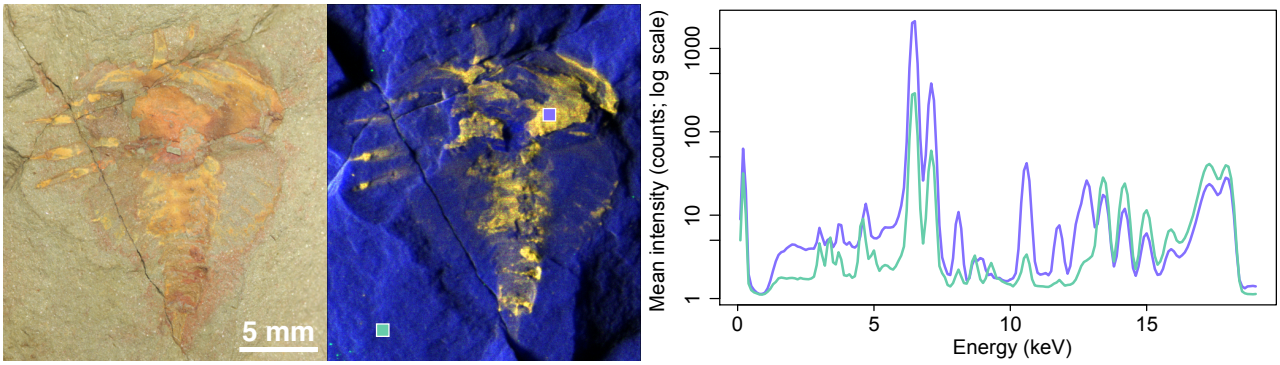

Figure S1. Synchrotron-based XRF major-to-trace elemental mapping of MGL 102701, an undescribed "xiphosuran" from the Early Ordovician Fezouata Shale of Morocco. Optical photograph (*left*), false-colour overlays of iron (red), manganese (green), and rubidium (blue) distributions (*centre*), and the extracted mean XRF spectra from box areas of corresponding colours in the elemental overlay (*right*). Refer to Fig. 1*O* for peak identification.

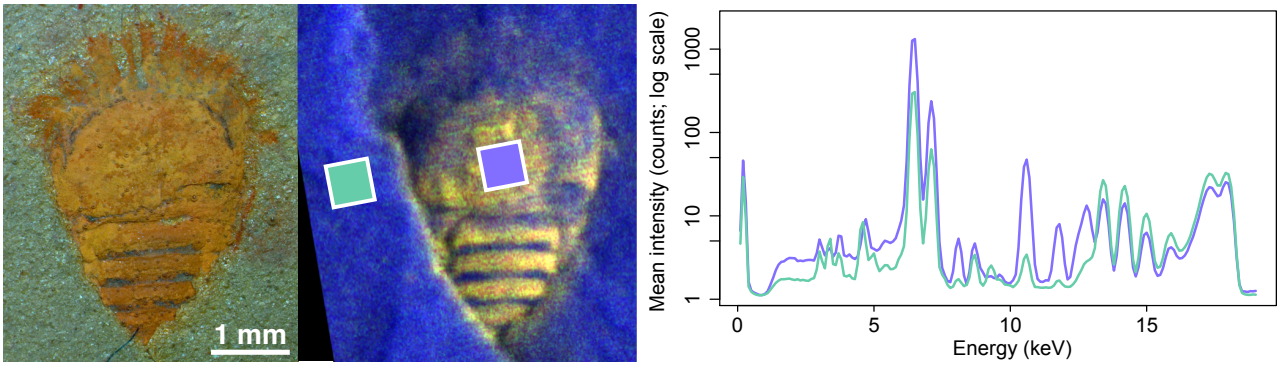

Figure S2. Synchrotron-based XRF major-to-trace elemental mapping of MGL 107210, an undescribed "synziphosurine" from the Early Ordovician Fezouata Shale of Morocco. Optical photograph (*left*), false-colour overlays of iron (red), manganese (green), and rubidium (blue) distributions (*centre*), and the extracted mean XRF spectra from box areas of corresponding colours in the elemental overlay (*right*). Refer to Fig. 1*O* for peak identification.

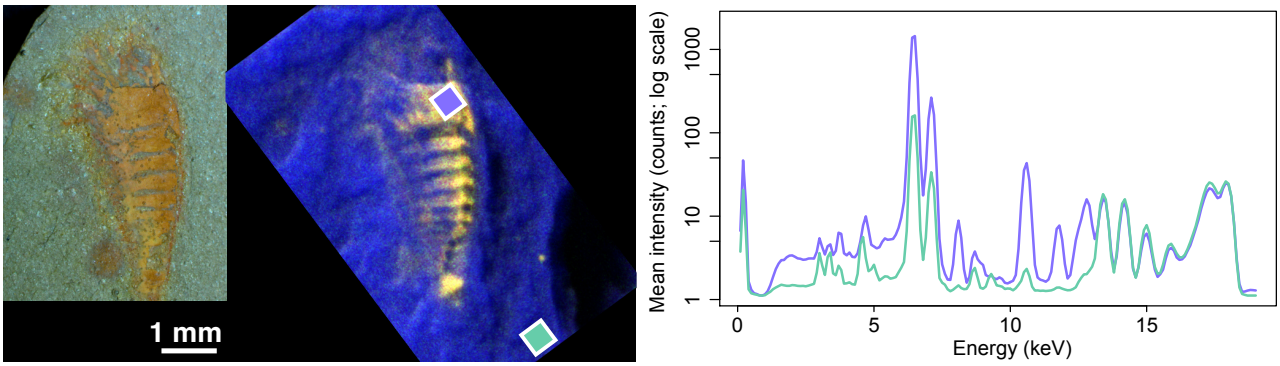

Figure S3. Synchrotron-based XRF major-to-trace elemental mapping of MGL 102841, an undescribed "synziphosurine" from the Early Ordovician Fezouata Shale of Morocco. Optical photograph (*left*), false-colour overlays of iron (red), manganese (green), and rubidium (blue) distributions (*centre*), and the extracted mean XRF spectra from box areas of corresponding colours in the elemental overlay (*right*). Refer to Fig. 1*O* for peak identification.

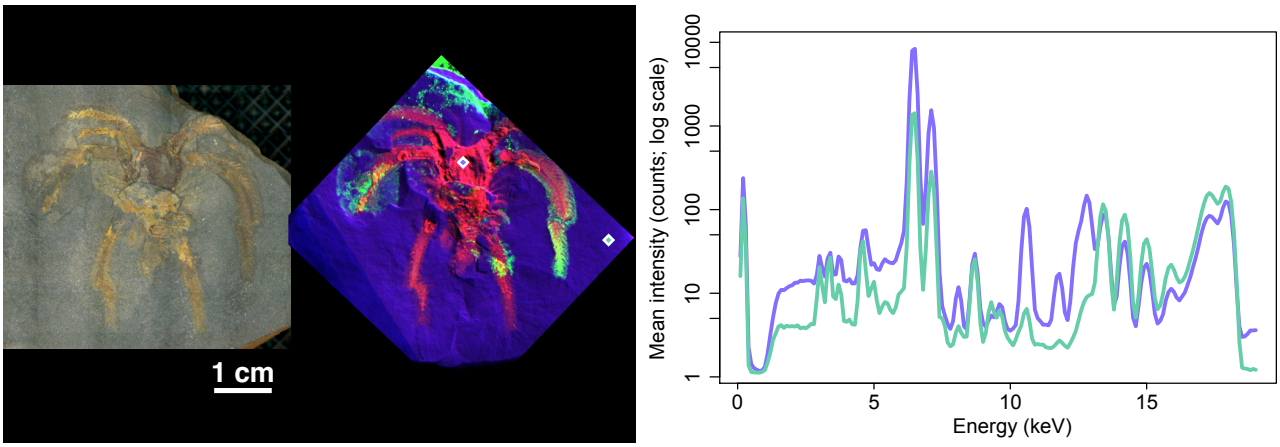

Figure S4. Synchrotron-based XRF major-to-trace elemental mapping of AA-BIZ31-OI-39, an undescribed "marrellid" from the Early Ordovician Fezouata Shale of Morocco. Optical photograph (*left*), false-colour overlays of iron (red), manganese (green), and rubidium (blue) distributions (*centre*), and the extracted mean XRF spectra from box areas of corresponding colours in the elemental overlay (*right*). Refer to Fig. 1*O* for peak identification.

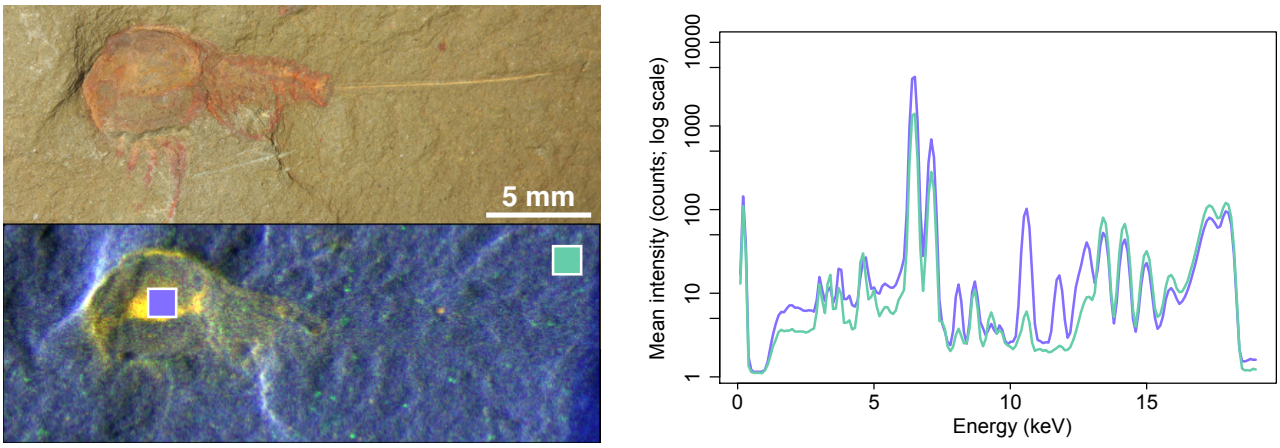

Figure S5. Synchrotron-based XRF major-to-trace elemental mapping of MGL 102705, an undescribed "xiphosuran" from the Early Ordovician Fezouata Shale of Morocco. Optical photograph (*top left*), false-colour overlays of iron (red), manganese (green), and rubidium (blue) distributions (*bottom left*), and the extracted mean XRF spectra from box areas of corresponding colours in the elemental overlay (*right*). Refer to Fig. 1*O* for peak identification.

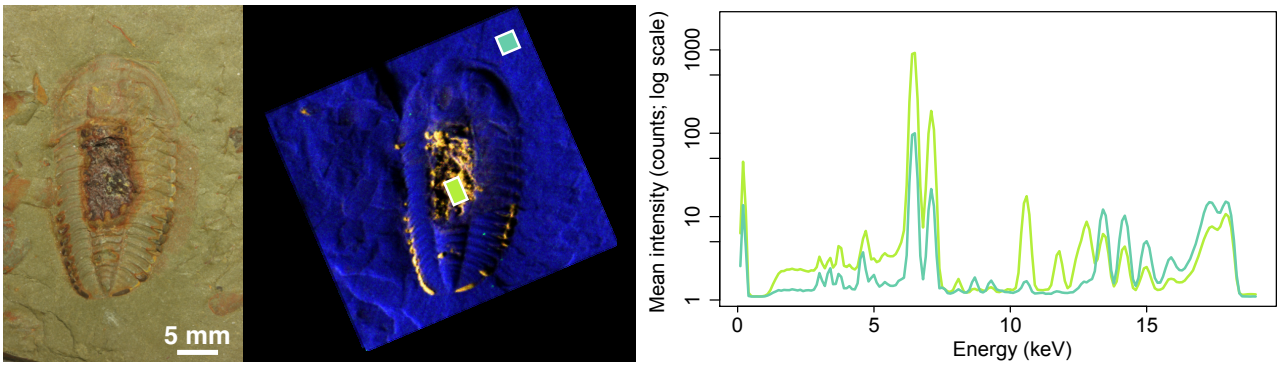

Figure S6. Synchrotron-based XRF major-to-trace elemental mapping of the trilobite *Bavarilla zemmourensis* Destombes, Sougy & Willefert, 1969, specimen MGL 102177, from the Early Ordovician Fezouata Shale of Morocco. Optical photograph (*left*), false-colour overlays of iron (red), manganese (green), and rubidium (blue) distributions (*centre*), and the extracted mean XRF spectra from box areas of corresponding colours in the elemental overlay (*right*). Refer to Fig. 1*O* for peak identification.

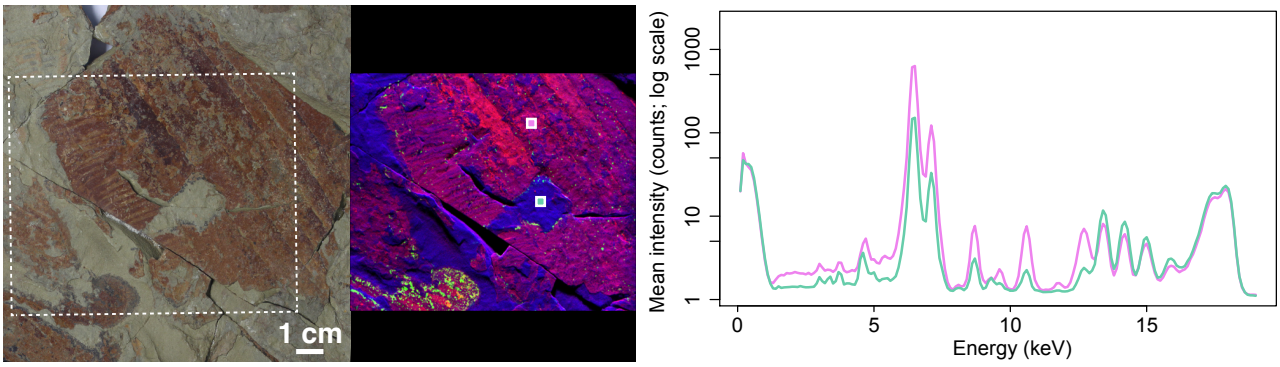

Figure S7. Synchrotron-based XRF major-to-trace elemental mapping of MGL 103593, undescribed "radiodont" appendages from the Early Ordovician Fezouata Shale of Morocco. Optical photograph (*left*), false-colour overlays of iron (red), manganese (green), and rubidium (blue) distributions (*centre*), and the extracted mean XRF spectra from box areas of corresponding colours in the elemental overlay (*right*). Refer to Fig. 1*O* for peak identification.

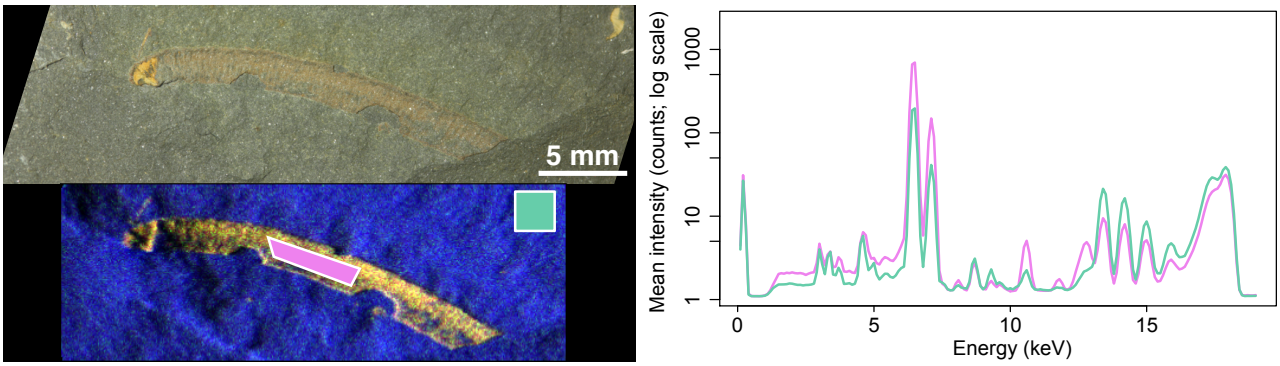

Figure S8. Synchrotron-based XRF major-to-trace elemental mapping of MGL 107866, an undescribed "annelid" from the Early Ordovician Fezouata Shale of Morocco. Optical photograph (*top left*), false-colour overlays of iron (red), manganese (green), and rubidium (blue) distributions (*bottom left*), and the extracted mean XRF spectra from box areas of corresponding colours in the elemental overlay (*right*). Refer to Fig. 1*O* for peak identification.

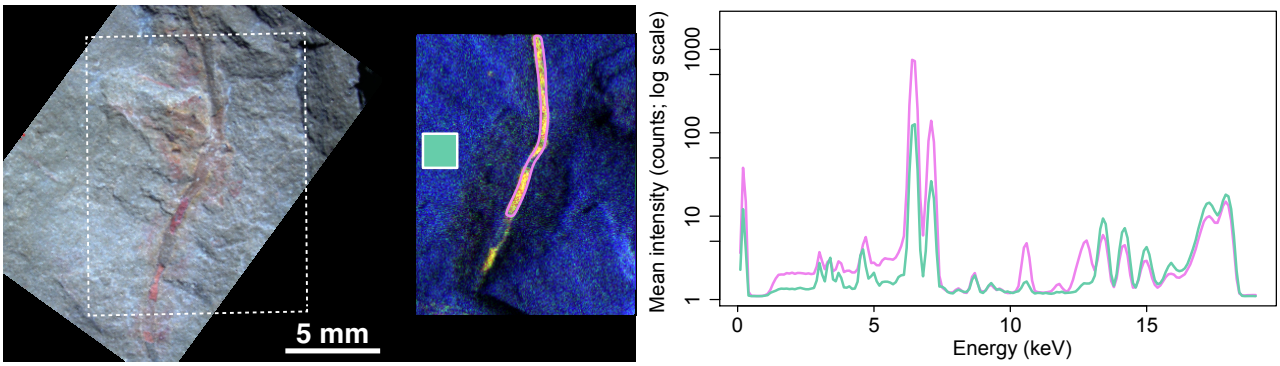

Figure S9. Synchrotron-based XRF major-to-trace elemental mapping of AA-TGR1c-OI-47, an undescribed "annelid" from the Early Ordovician Fezouata Shale of Morocco. Optical photograph (*left*), false-colour overlays of iron (red), manganese (green), and rubidium (blue) distributions (*centre*), and the extracted mean XRF spectra from selected areas of corresponding colours in the elemental overlay (*right*). Refer to Fig. 1*O* for peak identification.

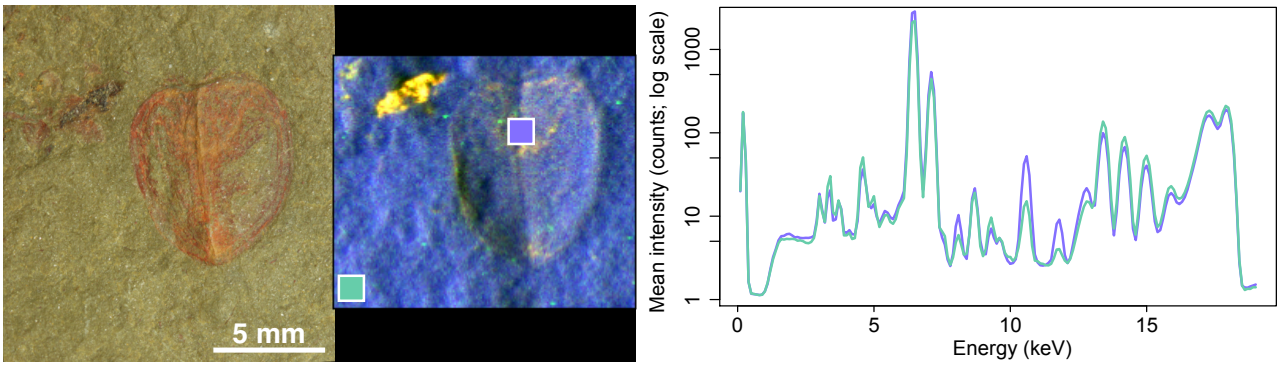

Figure S10. Synchrotron-based XRF major-to-trace elemental mapping of the marrellomorph euarthropod *Enosiaspis hrungnir* Legg, 2016, specimen MGL 102321, from the Early Ordovician Fezouata Shale of Morocco. Optical photograph (*left*), false-colour overlays of iron (red), manganese (green), and rubidium (blue) distributions (*centre*), and the extracted mean XRF spectra from box areas of corresponding colours in the elemental overlay (*right*). Refer to Fig. 1*O* for peak identification.

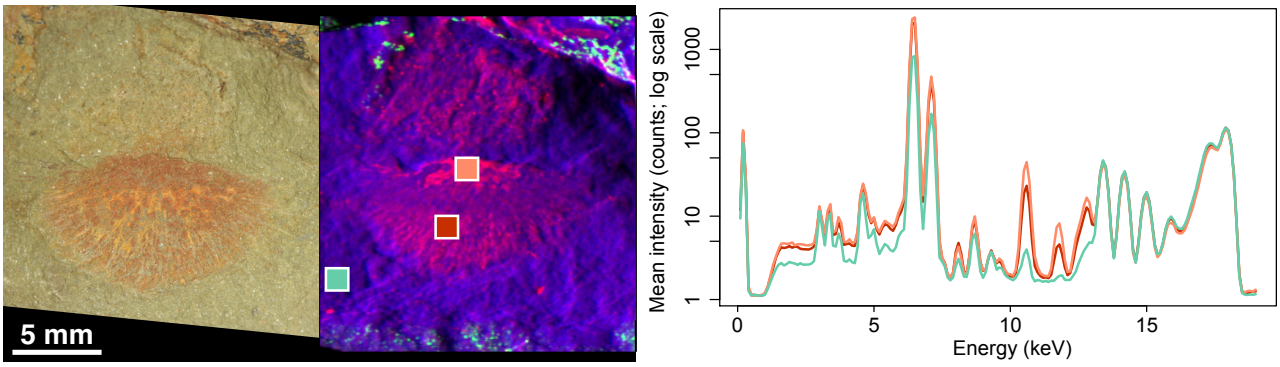

Figure S11. Synchrotron-based XRF major-to-trace elemental mapping of the demosponge *Choia sp.*, specimen MGL 107663, from the Early Ordovician Fezouata Shale of Morocco. Optical photograph (*left*), false-colour overlays of iron (red), manganese (green), and rubidium (blue) distributions (*centre*), and the extracted mean XRF spectra from box areas of corresponding colours in the elemental overlay (*right*). Refer to Fig. 1*O* for peak identification.

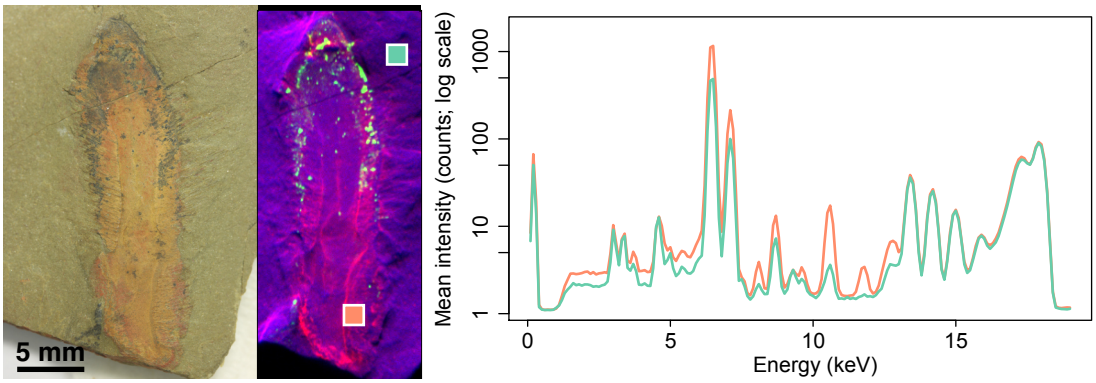

Figure S12. Synchrotron-based XRF major-to-trace elemental mapping of the demosponge *Pirania auraeum* Botting, 2007, specimen MGL 107764, from the Early Ordovician Fezouata Shale of Morocco. Optical photograph (*left*), false-colour overlays of iron (red), manganese (green), and rubidium (blue) distributions (*centre*), and the extracted mean XRF spectra from box areas of corresponding colours in the elemental overlay (*right*). Refer to Fig. 1*O* for peak identification.

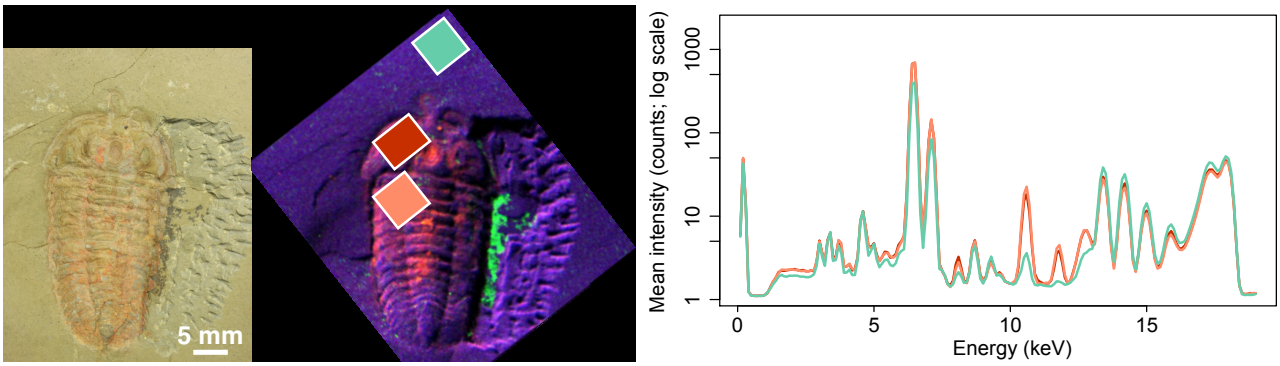

Figure S13. Synchrotron-based XRF major-to-trace elemental mapping of the trilobite *Bavarilla zemmourensis* Destombes, Sougy & Willefert, 1969, specimen MGL 102222, from the Early Ordovician Fezouata Shale of Morocco. Optical photograph (*left*), false-colour overlays of iron (red), manganese (green), and rubidium (blue) distributions (*centre*), and the extracted mean XRF spectra from box areas of corresponding colours in the elemental overlay (*right*). Refer to Fig. 1*O* for peak identification.

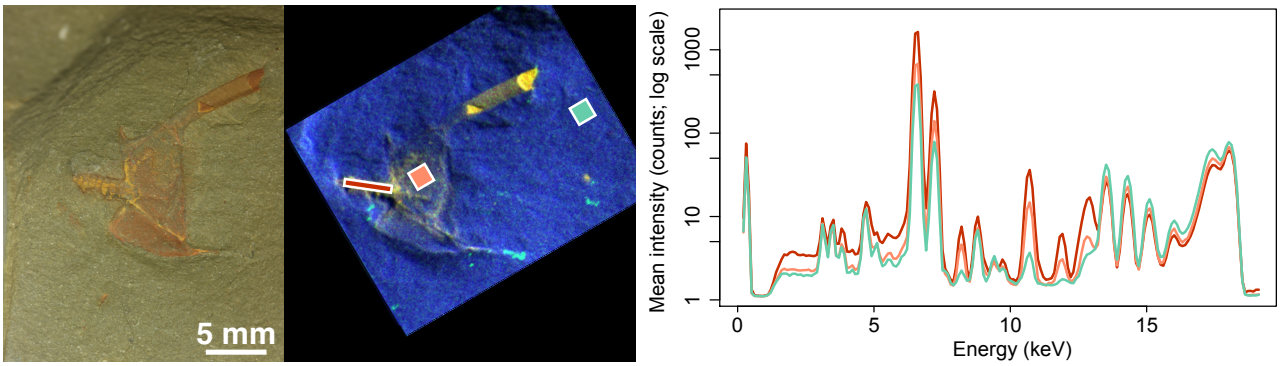

Figure S14. Synchrotron-based XRF major-to-trace elemental mapping of the stylophoran echinoderm *Thoralicystis sp.*, specimen MGL 107952, from the Early Ordovician Fezouata Shale of Morocco. Optical photograph (*left*), false-colour overlays of iron (red), manganese (green), and rubidium (blue) distributions (*centre*), and the extracted mean XRF spectra from box areas of corresponding colours in the elemental overlay (*right*). Refer to Fig. 1*O* for peak identification.

Figure S15. Satellite view of the Draa valley locating the different outcrops that yielded the fossils studied herein. The '~14km' measurement refers to the perimeter encompassing all the north localities. Precise locality information is curated with the specimens, and available upon request from the authors.

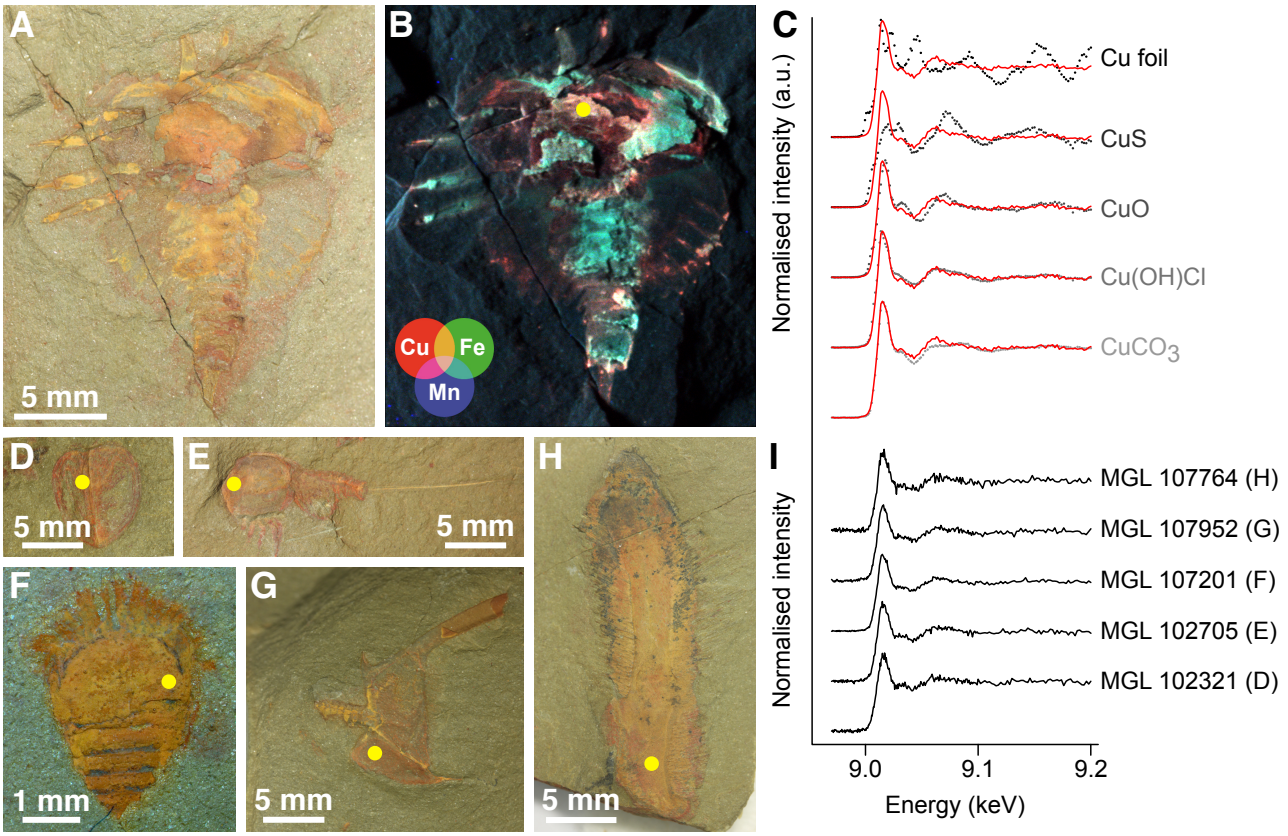

Figure S16. Synchrotron-based Cu K-edge X-ray absorption spectroscopy (XAS) of a range of fossils from the Early Ordovician Fezouata Shale of Morocco. (*A*) Optical photograph of the undescribed "xiphosuran" MGL 102701. (*B*) false-colour overlays of copper (red), iron (green), and manganese (blue) distributions. (*C*) Cu K-edge XAS spectrum (red line) from the yellow dot in *B* superimposed upon spectra collected on reference Cu compounds (grey to black dotted lines) for comparison. The spectrum obtained for the fossil is inconsistent with metallic copper (Cu), copper sulfide (CuS) or cupric oxide (CuO) but more consistent with copper hydroxide chloride (Cu(OH)Cl) and to a greater extent copper carbonate ($CuCO_3$), suggesting a similar environment for Cu in the fossil. (*D–H*) Optical photographs of *Enosiaspis hrungnir* MGL 102321 (*D*), the undescribed “xiphosuran" MGL 102705 (*E*), the undescribed "synziphosurine" MGL 107210 (*F*), *Thoralicystis sp.* MGL 107952 (*G*), and *Pirania auraeum* MGL 107764 (*H*). (*I*) Cu K-edge XAS spectra from the yellow dot in *D–H*, showing that Cu is present in all investigated fossils in the same chemical environment. XAS was performed at the DiffAbs beamline (SOLEIL synchrotron) with the following acquisition parameters: fluorescence mode, 230×150 μm^2 (H×V) beam spot size, 3 s counting time per energy step; energy step sizes were 0.5 eV between 8970 and 9030 eV, 1 eV between 9031 and 9100 eV, and 2 eV between 9102 and 9200 eV. Spectra have been normalised, and the references corrected from self-absorption, using the Athena software[68].

68. B. Ravel, M. Newville, ATHENA, ARTEMIS, HEPHAESTUS: data analysis for X-ray absorption spectroscopy using IFEFFIT. *Journal of Synchrotron Radiation* **12**, 537–541 (2005).

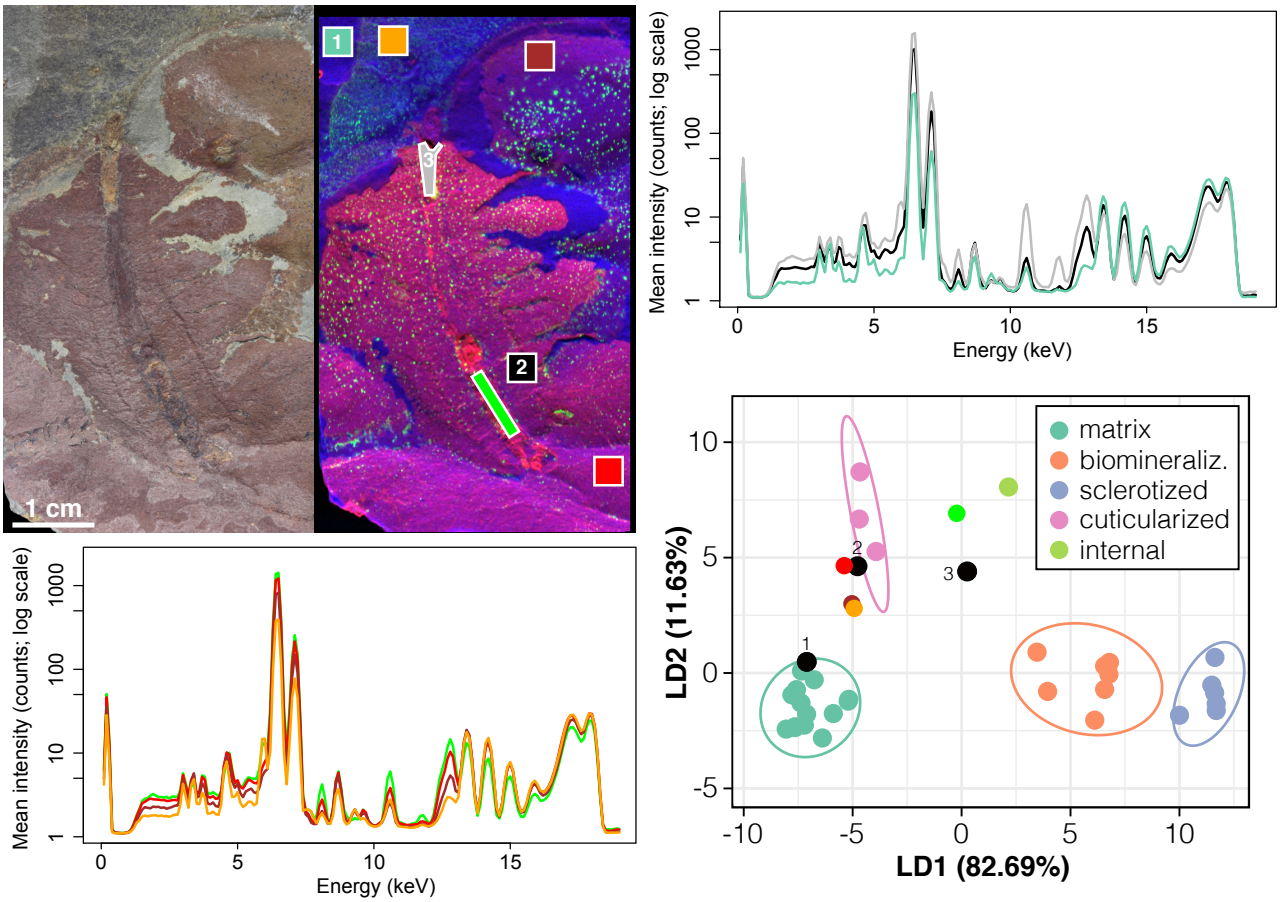

Figure S17. Synchrotron-based X-ray fluorescence major-to-trace elemental mapping of AA-FETB-OI-22, an undescribed "enigmatic organism" from the Early Ordovician Fezouata Shale of Morocco. (*Top left*) Optical photograph. (*Top centre*) False-colour overlays of iron (red), manganese (green), and rubidium (blue) distributions. (*Top right*) Mean XRF spectra from the box areas of corresponding colours (numbered 1 to 3) in the elemental overlay, corresponding to the same areas as in Fig. 2*C*. (*Bottom left*) Additional mean XRF spectra, extracted from the orange, brown, red (weathered matrix) and green (other internal remains) box areas of corresponding colours in the XRF false-colour overlay. Refer to Fig. 1*O* for peak identification. (*Bottom right*) Classification of the all 7 extracted XRF spectra within our linear discriminant analysis. Note that weathered matrix spectra plot closer to cuticularized tissues the richer they are in iron, following the fact that the shale matrix (clay and silica) is way less concentrated in iron than the fossil tissues (iron oxides). Of note is also the classification of the green XRF spectrum, corresponding to the remains of an internal system, which plots close to the trilobite internal, most likely digestive, tissue, suggesting that this area may preserve remains of the digestive system.

Taxon	Collection number	Locality	Figure(s)	Spectrum	Tissue type (Following [35])	XRF map scan step (µm)	XRF map dwell time (ms)	Number of pixels selected	Time over slected area (s)
undescribed "xiphosuran"	MGL 102701	A5 (2015)	Figs. 1*A*, S1	1	sclerotised	20	25	900	22.5
				2	matrix	20	25	900	22.5
undescribed "synziphosurine"	MGL 107210	A16 (2015)	Figs. 1*B*, S2	1	sclerotised	20	20	1122	22.44
				2	matrix	20	20	1122	22.44
undescribed "synziphosurine"	MGL 102841	"Synz. Loc."	Figs. 1*C,* S3	1	sclerotised	20	20	1122	22.44
				2	matrix	20	20	1122	22.44
undescribed "marrellid"	AA-BIZ31-OI-39	ZF4(31)	Figs. 1*D,* S4	1	sclerotised	70	70	324	22.68
				2	matrix	70	70	324	22.68
undescribed "xiphosuran"	MGL 102705	A5 (2015)	Figs. 1*E,* S5	1	sclerotised	70	50	441	22.05
				2	matrix	70	50	441	22.05
Bavarilla zemmourensis Destombes. Sougy & Willefert. 1969	MGL 102177	A17 (2015)	Figs. 1*F,* S6	1	internal	70	20	1128	22.56
				2	matrix	70	20	1122	22.44
undescribed "radiodont" appendages	MGL 103593	A27 (2016)	Figs. 1*G,* S7	1	cuticularised	70	25	900	22.5
				2	matrix	70	25	900	22.5
undescribed "annelid"	MGL 107866	A2 (2015)	Figs. 1*H,* S8	1	cuticularised	70	20	1127	22.54
				2	matrix	70	20	1122	22.44
undescribed "annelid"	AA-TGR1c-OI-47	ZF51c	Fig. S9	1	cuticularised	70	20	1124	22.48
				2	matrix	70	20	1122	22.44
Enosiaspis hrungnir Legg. 2016	MGL 102321	A6 (2015)	Figs. 1*I,* S10	1	sclerotised	70	60	380	22.8
				2	matrix	70	60	380	22.8
Choia sp. (Botting 2007)	MGL 107663	A17 (2015)	Figs. 1*J,* S11	1	biomineralised	70	50	441	22.05
				2	biomineralised	70	50	441	22.05
				3	matrix	70	50	441	22.05
Pirania auraeum Botting. 2007	MGL 107764	A26 (2016)	Figs. 1*K,* S12	1	biomineralised	70	40	552	22.08
				2	matrix	70	40	552	22.08

Bavarilla zemmourensis Destombes. Sougy & Willefert. 1969	MGL 102222	A16 (2015)	Figs. 1*L,* S13	1	biomineralised	200	20	1122	22.44
				2	biomineralised	200	20	858	17.16 **
				3	matrix	200	20	1122	22.44
Thoralicystis sp. (Lefebvre et al. 2019)	MGL 107952	A9 (2015)	Figs. 1*M,* S14	1	biomineralised	70	30	729	21.87
				2	biomineralised	70	30	638	19.14 **
				3	matrix	70	30	729	21.87
undescribed "enigmatic organism"	AA-FETB-OI-22	ZF2(3b)	Figs. 2, S17	1	?	100	20	1122	22.44
				2	?	100	20	1124	22.48
				3	matrix	100	20	1122	22.44
				4	weathered matrix	100	20	1122	22.44
				5	weathered matrix	100	20	1122	22.44
				6	weathered matrix	100	20	1122	22.44
				7	?	100	20	1121	22.42

Table S1. Details on the specimens. acquisition parameters and selected spectra studied herein. (** Denotes 2 spectra for which it was not possible to obtain a collection time over the selected area close to 22.5 s)

Element	Sclerotised	Biomineralised	Cuticularised
K	0.5112	1.956	0.4588
Ca	0.5725	0.5226	0.3237
Ti	0.1771	0.8605	0.2255
Cr	0.03413	0.04596	0.03328
Mn	0.2118	0.2076	0.2984
Ni	0.03054	0.03625	0.08007
Cu	0.3035	0.2087	0.02415
Zn	0.2127	0.4004	0.2436
Ga	0.007206	0.05585	0.01741
As	0.6792	0.522	0.04578
Br	0.006563	0.00397	0.0003272
Rb	0.2398	0.4184	0.1613
Sr	0.1391	0.2448	0.09511
Y	0.007973	0.03406	0.01968
Pb	0.5217	0.3441	0.3683

Table S2. XRF minor to trace element quantification of the mean spectra for the sclerotized, biomineralized and cuticularized tissues (wt%)